
A vertex scheme for two-phase flow in heterogeneous media

AN E-PRINT OF THE PAPER WILL BE MADE AVAILABLE ON ARXIV.

AUTHORED BY

M. S. JOSHAGHANI

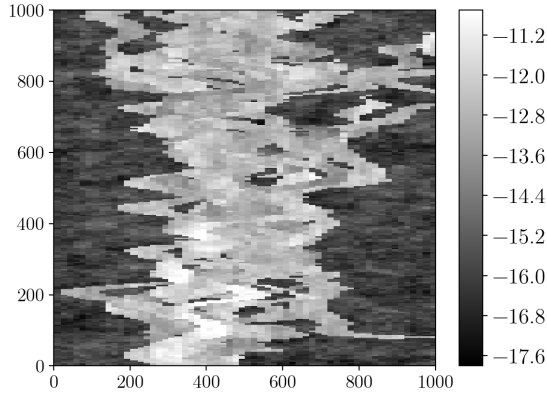
Postdoctoral Research Associate, Rice University, Houston, Texas 77005

V. GIRAULT

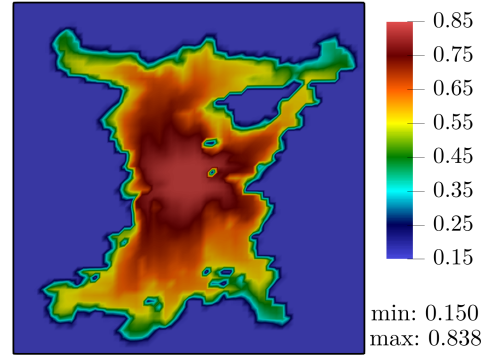
*Professor Emeritus, Laboratoire Jacques-Louis Lions
University Pierre et Marie Curie, France*

B. RIVIERE

*Noah Harding Chair and Professor of Computational and Applied Mathematics
Rice University, Houston, Texas 77005*



(a) Highly-varying permeability field (m^2) in logscale



(b) Wetting phase saturation; $t = 0.725$ days

Left figure shows a realistic discontinuous permeability field in a $1000\text{ m} \times 1000\text{ m}$ domain. Right figure shows the saturation profile obtained under the proposed finite element scheme. We observe that: (i) the permeability field determines the pattern fluid flows through porous media (ii) the proposed scheme exhibits satisfactory results with respect to maximum principle. This means that saturation solution always remains between s_{rw} and $1 - s_{ro}$ (between 0.15 and 0.85 in this problem).

A vertex scheme for two-phase flow in heterogeneous media

M. S. Joshaghani, V. Girault, and B. Riviere

ABSTRACT. This paper presents the numerical solution of immiscible two-phase flows in porous media, obtained by a first-order finite element method equipped with mass-lumping and flux upwinding. The unknowns are the physical phase pressure and phase saturation. Our numerical experiments confirm that the method converges optimally for manufactured solutions. For both structured and unstructured meshes, we observe the high-accuracy wetting saturation profile that ensures minimal numerical diffusion at the front. Performing several examples of quarter-five spot problems in two and three dimensions, we show that the method can easily handle heterogeneities in the permeability field. Two distinct features that make the method appealing to reservoir simulators are: (i) maximum principle is satisfied, and (ii) mass balance is locally conserved.

1. INTRODUCTION

A first-order finite element method is proposed to simulate two-phase flows in heterogeneous porous media. The method is defined for unstructured meshes made of simplices for two-dimensional or three-dimensional domains. Mass-lumping and upwinding techniques are employed to discretize the mass and stiffness matrices. The proposed method solves for primary unknowns that are physical quantities, namely the wetting phase pressure and the wetting phase saturation. Flows are driven by injection and production wells, represented by source and sink functions. The method has recently been analyzed in the papers by [Girault et al. \[2020a,b\]](#). The fact that the relative permeabilities vanish when evaluated at the residual saturation values and that the capillary pressure has an unbounded derivative make the proofs for the well-posedness and convergence analysis of the scheme technical and complicated. In this current work, we extend the scheme to heterogeneous porous media for which the permeability field varies over several orders of magnitude across the domain. Several simulations of incompressible two-phase flow in two-dimensional and three-dimensional domains show the accuracy and robustness of the proposed mass-lumped upwinded finite element method. In this paper, our proposed scheme will be referred to as the “vertex scheme” because mass-lumping reduces the finite element integrals to quantities involving the values of the solution at the vertices. Thanks to the use of mass-lumping and upwinding, the maximum principle is proved and observed in our computations. The numerical solution of the saturation does not exhibit local oscillations near the front, which indicates the monotonicity of the scheme.

The numerical modeling of incompressible two-phase flow in porous media has been widely studied in the literature. Only a small fraction of the proposed schemes with physical primary unknowns, has been theoretically analyzed. Besides our proposed finite element method [[Girault et al., 2020a,b](#)], a cell-centered finite volume method has been analyzed in [[Eymard et al., 2003](#)]. Many of the convergence works in the literature impose unrealistic constraints on the input data, in

particular the relative permeabilities are assumed to be bounded below by positive constants and the derivative of the capillary pressure is assumed to be bounded [Ohlberger, 1997; Epshteyn and Riviere, 2009; Eymard et al., 2014]. If non-physical primary unknowns are chosen, such as the global pressure introduced by Chavent and Jaffré [1986], the degeneracy of the relative permeabilities can be circumvented (see [Douglas, 1983; Michel, 2003; Chen and Ewing, 2001]). The idea of using mass-lumping has been proposed for the numerical solution of various partial differential equations (see for instance [Chen and Thomée, 1985; Cohen et al., 2001]) as well as in the application of porous media (see [Forsyth, 1991; Abriola and Rathfelder, 1993]). Mass-lumping within the finite element method yields a diagonal mass matrix, which is a desirable feature for reducing the computational cost. Upwinding helps reducing the numerical oscillations near fronts in convection-dominated problems.

An outline of the paper follows. In Section 2, the two-phase flow model is presented with wetting phase saturation and pressure as primary unknowns. The vertex scheme is defined in Section 3 and the resulting linearized system is described in Section 4. Numerical simulations are shown in Section 5 and are followed by conclusions.

2. GOVERNING EQUATIONS

The incompressible two-phase flow model in a porous medium $\Omega \subset \mathbb{R}^d$, $d = 2, 3$, over a time interval $(0, T)$ is characterized by the following coupled equations:

$$\partial_t(\phi s) - \nabla \cdot (\eta_w(s) K \nabla p) = f_w(s_{\text{in}}) \bar{q} - f_w(s) \underline{q}, \quad \text{in } \Omega \times (0, T), \quad (2.1a)$$

$$-\partial_t(\phi s) - \nabla \cdot (\eta_o(s) K (\nabla p_c(s) + \nabla p)) = f_o(s_{\text{in}}) \bar{q} - f_o(s) \underline{q}, \quad \text{in } \Omega \times (0, T), \quad (2.1b)$$

$$\eta_w(s) K \nabla p \cdot \mathbf{n} = 0, \quad \text{on } \partial\Omega \times (0, T), \quad (2.1c)$$

$$\eta_o(s) K \nabla p_o \cdot \mathbf{n} = 0, \quad \text{on } \partial\Omega \times (0, T). \quad (2.1d)$$

The primary unknowns are the wetting phase pressure, p , and wetting phase saturation, s . The secondary unknowns, namely the non-wetting phase pressure and saturation, (p_o, s_o) , are recovered by using the relations:

$$p_o = p_c(s) + p, \quad s_o = 1 - s.$$

The porosity and the permeability of the medium are denoted by ϕ and K respectively. The mobilities, η_α , are the ratios of the relative permeabilities, $k_{r\alpha}$, to the phase viscosities, $\mu_\alpha > 0$, for $\alpha = o, w$:

$$\eta_\alpha(s) = \frac{k_{r\alpha}(s)}{\mu_\alpha}, \quad \alpha = w, o. \quad (2.2)$$

Both capillary pressure, p_c , and relative permeabilities are functions of the saturation (see [Brooks and Corey, 1964; Genuchten, 1980]). In this work, the Brooks-Corey model is used. The residual saturations, s_{rw}, s_{ro} , are constants in the interval $[0, 1]$.

$$k_{rw}(s) = \bar{s}^{\frac{2+3\theta}{\theta}}, \quad k_{ro}(s) = (1 - \bar{s})^2 (1 - \bar{s}^{\frac{2+3\theta}{\theta}}), \quad \bar{s} = \frac{s - s_{rw}}{1 - s_{rw} - s_{ro}}, \quad (2.3)$$

$$p_c(s) = \begin{cases} p_d \bar{s}^{-\frac{1}{\theta}} & \text{if } \bar{s} > R \\ p_d R^{-\frac{1}{\theta}} - \frac{p_d}{\theta} R^{(-1-\frac{1}{\theta})} (\bar{s} - R) & \text{otherwise.} \end{cases} \quad (2.4)$$

This model introduces a parameter $\theta \in [0.2, 3.0]$, which characterizes the inhomogeneity of the medium. The entry pressure, p_d , is a constant pressure corresponding to the capillary pressure

required to displace the fluid from the largest pore. The fractional flows of each phase are related to the mobilities as follows:

$$f_w(s) = \frac{\eta_w(s)}{\eta_w(s) + \eta_o(s)}, \quad f_o(s) = 1 - f_w(s). \quad (2.5)$$

Flow rates at the injection and production wells, \bar{q} , and \underline{q} satisfy:

$$\bar{q} \geq 0, \quad \underline{q} \geq 0, \quad \int_{\Omega} \bar{q} = \int_{\Omega} \underline{q}, \quad (2.6)$$

and the saturation at the injection wells is set equal to a constant value s_{in} . Finally the model is completed by the initial condition:

$$s = s^0, \quad \text{in } \Omega. \quad (2.7)$$

3. NUMERICAL SCHEME

The domain Ω is partitioned into triangular elements in 2D and tetrahedral elements in 3D. Let h denote the maximum diameter of each element in the mesh \mathcal{E}_h . Let τ denote the time step size and let p_h^n, s_h^n denote the discrete pressure and saturation respectively at time $t^n = n\tau$. They belong to the finite element space X_h of order one:

$$X_h = \{v_h \in \mathcal{C}^0(\bar{\Omega}) : \forall E \in \mathcal{E}_h, v_h|_E \in \mathbb{P}_1(E)\}.$$

Let M be the dimension of X_h ; it is the number of nodes (i.e. vertices) of \mathcal{E}_h . Let Φ_i be the Lagrange basis function, that is piecewise linear and takes the value 1 at node i and 0 at all the other nodes. We write

$$p_h^n(\mathbf{x}) = \sum_{i=1}^M P_i^n \Phi_i(\mathbf{x}), \quad s_h^n(\mathbf{x}) = \sum_{i=1}^M S_i^n \Phi_i(\mathbf{x}), \quad \mathbf{x} \in \Omega. \quad (3.1)$$

We now define coefficients that arise from the mass-lumping technique. For a fixed node i , the macro-element Δ_i is defined as the union of elements sharing the node i .

$$c_{ij,E} = \int_E |\nabla \Phi_i \cdot \nabla \Phi_j|, \quad c_{ij} = \sum_{E \in \Delta_i \cap \Delta_j} c_{ij,E}, \quad c_{ij}(K) = \sum_{E \in \Delta_i \cap \Delta_j} K_E c_{ij,E}, \quad \forall 1 \leq i, j \leq M,$$

$$m_i = \frac{|\Delta_i|}{d+1}, \quad \forall 1 \leq i, j \leq M.$$

We assume here that the permeability K is piecewise constant and we denote by K_E the constant value that is the restriction of K on the element E . Clearly, if K is constant everywhere, then $c_{ij}(K) = K c_{ij}$.

We first introduce the nonlinear scheme, that is written with respect to the nodal values of the numerical pressure and saturation. For $n \geq 1$, given $s_h^{n-1} \in X_h$, find $(p_h^n, s_h^n) \in X_h \times X_h$ satisfying (3.1) and

$$\begin{aligned} & m_i \phi \frac{S_i^n - S_i^{n-1}}{\tau} - \sum_{j=1}^M c_{ij}(K) \eta_w(S_{w,ij}^n) (P_j^n - P_i^n) \\ & = m_i (f_w(s_{\text{in}}) \bar{q}_i - f_w(S_i^{n-1}) \underline{q}_i), \quad 1 \leq i \leq M-1, \end{aligned} \quad (3.2)$$

$$\begin{aligned}
& -m_i \phi \frac{S_i^n - S_i^{n-1}}{\tau} - \sum_{j=1}^M c_{ij}(K) \eta_o(S_{o,ij}^n) (P_j^n - P_i^n) \\
& - \sum_{j=1}^M c_{ij}(K) \eta_o(S_{o,ij}^n) \left(p_c(S_j^{n-1}) + p'_c(S_j^{n-1})(S_j^n - S_j^{n-1}) - p_c(S_i^{n-1}) - p'_c(S_i^{n-1})(S_i^n - S_i^{n-1}) \right) \\
& = m_i (f_o(s_{\text{in}}) \bar{q}_i - f_o(S_i^{n-1}) \underline{q}_i), \quad 1 \leq i \leq M,
\end{aligned} \tag{3.3}$$

$$\sum_{i=1}^M m_i P_i^n = 0. \tag{3.4}$$

The values $S_{w,ij}^n$ and $S_{o,ij}^n$ are upwind values, i.e. they are nodal values of the saturation at either node i or node j , that are made precise in the linearized scheme below. In the case of constant permeability, well-posedness and convergence of the nonlinear scheme are proved in [Girault et al., 2020a,b].

PROPOSITION 3.1. *Let (s, p) be a weak solution to problem (2.1a)-(2.1b). Assume that the porosity ϕ and permeability K are positive constants. As the mesh size h and time step size τ tend to zero, the discrete saturation satisfying (3.2)-(3.4) converges, up to a subsequence, strongly to s in the L^2 norm and the discrete pressure converges, up to a subsequence, weakly to p . In addition, the saturation satisfies the maximum principle:*

$$s_{rw} \leq s_h^n(\mathbf{x}) \leq 1 - s_{ro}, \quad \forall \mathbf{x} \in \Omega. \tag{3.5}$$

Linearized Scheme: We linearize the equations (3.2)-(3.3) by using a fixed point iteration and approximating the capillary pressure by a first-order Taylor expansion:

$$p_c(S_i^n) \approx p_c(S_i^{n-1}) + p'_c(S_i^{n-1})(S_i^n - S_i^{n-1}).$$

At each time step t^n , we will solve for a sequence of nodal values $(P_i^{n,k}, S_i^{n,k})$ where the superscript k denotes the fixed-point iteration number.

$$\begin{aligned}
& m_i \phi \frac{S_i^{n,k} - S_i^{n-1}}{\tau} - \sum_{j=1}^M c_{ij}(K) \eta_w(S_{w,ij}^{n,k-1}) (P_j^{n,k} - P_i^{n,k}) \\
& = m_i (f_w(s_{\text{in}}) \bar{q}_i - f_w(S_i^{n-1}) \underline{q}_i), \quad 1 \leq i \leq M-1, \\
& -m_i \phi \frac{S_i^{n,k} - S_i^{n-1}}{\tau} - \sum_{j=1}^M c_{ij}(K) \eta_o(S_{o,ij}^{n,k-1}) (P_j^{n,k} - P_i^{n,k}) \\
& - \sum_{j=1}^M c_{ij}(K) \eta_o(S_{o,ij}^{n,k-1}) \left(p_c(S_j^{n-1}) + p'_c(S_j^{n-1})(S_j^{n,k} - S_j^{n-1}) - p_c(S_i^{n-1}) - p'_c(S_i^{n-1})(S_i^{n,k} - S_i^{n-1}) \right) \\
& = m_i (f_o(s_{\text{in}}) \bar{q}_i - f_o(S_i^{n-1}) \underline{q}_i), \quad 1 \leq i \leq M,
\end{aligned} \tag{3.6}$$

$$\tag{3.7}$$

$$\sum_{i=1}^M m_i P_i^{n,k} = 0. \quad (3.8)$$

We now make precise the choice of the upwind values, $S_{w,ij}^{n,k}$ and $S_{o,ij}^{n,k}$:

$$S_{w,ij}^{n,k-1} = \begin{cases} S_i^{n,k-1} & \text{if } P_i^{n,k-1} > P_j^{n,k-1} \\ S_j^{n,k-1} & \text{if } P_i^{n,k-1} < P_j^{n,k-1} \\ \max(S_i^{n,k-1}, S_j^{n,k-1}) & \text{if } P_i^{n,k-1} = P_j^{n,k-1}, \end{cases} \quad (3.9)$$

$$S_{o,ij}^{n,k-1} = \begin{cases} S_i^{n,k-1} & \text{if } p_c(S_i^{n,k-1}) + P_i^{n,k-1} > p_c(S_j^{n,k-1}) + P_j^{n,k-1} \\ S_j^{n,k-1} & \text{if } p_c(S_i^{n,k-1}) + P_i^{n,k-1} < p_c(S_j^{n,k-1}) + P_j^{n,k-1} \\ \min(S_i^{n,k-1}, S_j^{n,k-1}) & \text{if } p_c(S_i^{n,k-1}) + P_i^{n,k-1} = p_c(S_j^{n,k-1}) + P_j^{n,k-1}. \end{cases} \quad (3.10)$$

We initialize the iterates with the values at the previous time-step:

$$P_i^{n,0} = P_i^{n-1}, \quad S_i^{n,0} = S_i^{n-1}.$$

Convergence is obtained when the difference between two iterates for both discrete pressure and saturation is small (less than 10^{-5}) in the L^∞ norm. The nodal values of the saturation and pressure at time t^n are the nodal values of the converged iterates. Since the finite element solutions s_h^n and p_h^n uniquely depend on the nodal values, they can be evaluated at any point in the domain.

Finally, to start the algorithm, we choose for s_h^0 the Lagrange interpolant of the saturation s_0 and for p_h^0 a constant value so that $S_{w,ij}^{0,0}$ and $S_{o,ij}^{0,0}$ are well defined.

REMARK 3.1. Equation (3.6) is valid for $i = M$; this can be obtained by adding (3.6) and (3.7) and by using (3.8).

4. SOLVER METHODOLOGY

The fully discrete formulations (3.6)-(3.8) yield a 2×2 block linear system of the form:

$$\begin{pmatrix} \mathbf{K}_{ss} & \mathbf{K}_{sp} \\ \mathbf{K}_{ps} & \mathbf{K}_{pp} \end{pmatrix} \begin{pmatrix} \mathbf{s} \\ \mathbf{p} \end{pmatrix} = \begin{pmatrix} \mathbf{f}_s \\ \mathbf{f}_p \end{pmatrix} \quad (4.1)$$

where each block is of size $M \times M$ and has entries that depend on the time step and the Picard iterate. Because of the local support of the basis functions, the sums over all the nodes in (3.6) and (3.7) reduce to sums over a small set of nodes, which leads to sparse matrices. To be precise, let $\mathcal{N}(i)$ be the set of indices of all nodes in the macro-element Δ_i .

The block \mathbf{K}_{ss} is a diagonal matrix:

$$(\mathbf{K}_{ss})_{ii} = \frac{m_i \phi}{\tau}, \quad 1 \leq i \leq M-1, \quad (\mathbf{K}_{ss})_{MM} = 0.$$

The non-zero entries in the block \mathbf{K}_{sp} are:

$$(\mathbf{K}_{sp})_{ij} = -c_{ij}(K)\eta_w(S_{w,ij}^{n,k-1}), \quad 1 \leq i \leq M-1, j \in \mathcal{N}(i), j \neq i, \quad (\mathbf{K}_{sp})_{ij} = m_j, \quad i = M, 1 \leq j \leq M.$$

The non-zero entries in the block \mathbf{K}_{ps} are:

$$(\mathbf{K}_{ps})_{ii} = -\frac{m_i \phi}{\tau}, \quad 1 \leq i \leq M, \quad (\mathbf{K}_{ps})_{ij} = -c_{ij}(K)\eta_o(S_{o,ij}^{n,k-1})p'_c(S_j^{n-1}), \quad 1 \leq i \leq M, j \in \mathcal{N}(i), j \neq i.$$

The non-zero entries in the block \mathbf{K}_{pp} are:

$$(\mathbf{K}_{pp})_{ij} = -c_{ij}(K)\eta_o(S_{o,ij}^{n,k-1}), \quad 1 \leq i \leq M, j \in \mathcal{N}(i), j \neq i.$$

For completeness, we display the entries of the right-hand side vectors \mathbf{f}_s and \mathbf{f}_p .

$$\begin{aligned} (\mathbf{f}_s)_i &= \frac{m_i \phi}{\tau} + m_i(f_w(s_{\text{in}})\bar{q}_i - f_w(S_i^{n-1})\underline{q}_i), \quad 1 \leq i \leq M-1, \quad (\mathbf{f}_s)_M = 0, \\ (\mathbf{f}_p)_i &= -\frac{m_i \phi}{\tau} + m_i(f_o(s_{\text{in}})\bar{q}_i - f_o(S_i^{n-1})\underline{q}_i) \\ &\quad + \sum_{j \in \mathcal{N}(i)} c_{ij}\eta_o(S_{o,ij}^{n,k-1}) \left(p_c(S_j^{n-1}) - p'_c(S_j^{n-1})S_j^{n-1} - p_c(S_i^{n-1}) + p'_c(S_i^{n-1})S_i^{n-1} \right). \end{aligned} \quad (4.2)$$

It is worth noting that the construction of the global matrix \mathbf{K} is done by assembling local matrices, as this is usually done in the finite element framework. For example we describe the procedure for assembling the block \mathbf{K}_{ps} in Algorithm 1; the other blocks \mathbf{K}_{ss} , \mathbf{K}_{sp} , and \mathbf{K}_{pp} are handled similarly. Let \mathbf{C}_{loc}^E be the local matrix associated with the c_{ij} coefficients restricted to an element E .

$$(\mathbf{C}_{loc}^E)_{i_{loc},j_{loc}} = \int_E |\nabla \Psi_{i_{loc}} \cdot \nabla \Psi_{j_{loc}}|, \quad \forall 1 \leq i_{loc}, j_{loc} \leq d+1,$$

where the functions $\Psi_{i_{loc}}$ are linear polynomials on E that correspond to the restriction of a global basis Φ_i on E for the node i with local number equal to i_{loc} .

REMARK 4.1. *In the case of a two-dimensional domain partitioned into a structured mesh of right-triangular elements of size h , the local matrix \mathbf{C}_{loc}^E is the same constant matrix for all elements E . Taking the local numbering counterclockwise and start from the right-angle node, \mathbf{C}_{loc}^E reads as follows:*

$$\mathbf{C}_{loc}^E = \begin{pmatrix} 0.5 & 0.5 & 0.5 \\ 0.5 & 0.5 & 0.0 \\ 0.5 & 0.0 & 0.5 \end{pmatrix}, \quad \forall E \in \mathcal{E}_h. \quad (4.3)$$

However, for unstructured meshes, the entries of the local matrix will depend on the element.

A Schur complement approach is used to factorize the matrix \mathbf{K} following [Mapakshi et al., 2018; Joshaghani et al., 2019] and the references within can be applied. Since the block \mathbf{K}_{ss} is not invertible, we rewrite the system \mathbf{K} as

$$\mathbf{K} = \begin{pmatrix} \mathbf{A}_{11} & \mathbf{A}_{12} \\ \mathbf{A}_{21} & \mathbf{A}_{22} \end{pmatrix},$$

where $\mathbf{A}_{11} = \mathbf{K}_{ss}(1 : M-1, 1 : M-1)$. In other words, we shifted the definition of the blocks so that the first block \mathbf{A}_{11} is of size $(M-1) \times (M-1)$ and it is now invertible. We now write

$$\mathbf{K} = \begin{pmatrix} \mathbf{I} & \mathbf{0} \\ \mathbf{A}_{21}(\mathbf{A}_{11})^{-1} & \mathbf{I} \end{pmatrix} \begin{pmatrix} \mathbf{A}_{11} & \mathbf{0} \\ \mathbf{0} & \mathbf{S} \end{pmatrix} \begin{pmatrix} \mathbf{I} & (\mathbf{A}_{11})^{-1}\mathbf{A}_{12} \\ \mathbf{0} & \mathbf{I} \end{pmatrix}, \quad (4.4)$$

where \mathbf{I} is the identity matrix and

$$\mathbf{S} = \mathbf{A}_{22} - \mathbf{A}_{21}(\mathbf{A}_{11})^{-1}\mathbf{A}_{12} \quad (4.5)$$

Algorithm 1 Assembly for \mathbf{K}_{ps} matrix at time step t^n and Picard's iteration k .

Input: $(S_i^{n-1})_i, (S_i^{n,k-1})_i, (P_i^{n,k-1})_i$.

Initialize \mathbf{K}_{ps} to the zero matrix.

for each element E in mesh **do**

 construct \mathbf{C}_{loc}^E

\triangleright For structured mesh: \mathbf{C}_{loc}^E is constant over all elements

 evaluate $K_E = K|_E$

\triangleright Value of permeability in element E .

for $i_{loc} = \{1, 2, \dots, d+1\}$ **do**

\triangleright There are $(d+1)$ degrees-of-freedom per element

$i = \text{glodofs}(i_{loc})$

\triangleright Global number of local node

$\mathbf{K}_{ps}(i, i) = -\frac{\phi|E|}{(d+1)\tau}$

\triangleright Mass-lumping operation

for $j_{loc} = \{1, 2, \dots, d+1\} \setminus \{i_{loc}\}$ **do**

$j = \text{glodofs}(j_{loc})$

\triangleright Global number of local node

if $p_c(S_i^{n,k-1}) + P_i^{n,k-1} > p_c(S_j^{n,k-1}) + P_j^{n,k-1}$ **then**

\triangleright Upwinding operation

$\text{Eta}_{ij} = \eta_o(S_i^{n,k-1})$

else if $p_c(S_i^{n,k-1}) + P_i^{n,k-1} < p_c(S_j^{n,k-1}) + P_j^{n,k-1}$ **then**

$\text{Eta}_{ij} = \eta_o(S_j^{n,k-1})$

else

$\text{Eta}_{ij} = \eta_o(\min(S_i^{n,k-1}, S_j^{n,k-1}))$

end if

$\mathbf{K}_{ps}(i, j) = -\text{Eta}_{ij} \times \mathbf{C}_{loc}^E(i_{loc}, j_{loc}) \times K_E \times \frac{dp_c}{ds}(S_j^{n-1})$

end for

end for

end for

is the Schur complement. The inverse can therefore be written as:

$$\mathbf{K}^{-1} = \begin{pmatrix} \mathbf{I} & -(\mathbf{A}_{11})^{-1}\mathbf{A}_{12} \\ \mathbf{0} & \mathbf{I} \end{pmatrix} \begin{pmatrix} (\mathbf{A}_{11})^{-1} & \mathbf{0} \\ \mathbf{0} & \mathbf{S}^{-1} \end{pmatrix} \begin{pmatrix} \mathbf{I} & \mathbf{0} \\ -\mathbf{A}_{21}(\mathbf{A}_{11})^{-1} & \mathbf{I} \end{pmatrix}. \quad (4.6)$$

The task at hand is to find the inverse of \mathbf{S} . Note that \mathbf{A}_{11} is a diagonal mass matrix for the saturation equation and hence it is straightforward to obtain the inverse. For the Schur complement block we employ the multigrid V-cycle on \mathbf{S} from the HYPRE boomerAMG package [Falgout and Yang, 2002]. We expect this to work since the \mathbf{S} block is spectrally equivalent to the Laplacian. When the inverses are obtained, we rely on GMRES [Saad and Schultz, 1986] with relative tolerance of 1×10^{-8} to solve the entire block system. It is found in [Mapakshi et al., 2018] that this methodology is computationally less expensive and more practical for large-scale computations. Solving the system of equations (4.1) in fast and efficient way can be done through PETSc [Balay et al., 2017, 2018; Dalcin et al., 2011] and its composable solver capabilities [Brown et al., 2012]. Appendix 6 contains the necessary PETSc command-line options for the described Schur complement approach. All the numerical results are generated using FEniCS Project [Logg and Wells, 2010; Brooks and Corey, 1964]. Among the various components available in FEniCS, we use the DOLFIN library [Logg et al., 2012] and the Unified Form Language library [S. Alnæs, 2012]. Simulations are conducted on a single socket Intel Core i7-7920HQ server node by utilizing a single MPI process. Computer codes implementing the proposed computational framework can be found at ZENODO/Vertex-based-method [2021].

TABLE 1. Results of convergence test where the mesh size is denoted by h . The time step τ is set to mesh size and L^2 and H^1 norms are computed at the final time $T = 1$

h	M	τ	$\ s_h - s\ _{L^2(\Omega)}$		$\ p_h - p\ _{L^2(\Omega)}$		$\ s_h - s\ _{H^1(\Omega)}$		$\ p_h - p\ _{H^1(\Omega)}$	
			Error	Rate	Error	Rate	Error	Rate	Error	Rate
1/4	25	1/4	9.430×10^{-4}	—	8.830×10^{-3}	—	5.160×10^{-3}	—	4.980×10^{-2}	—
1/8	81	1/8	6.600×10^{-4}	0.515	4.740×10^{-3}	0.899	3.610×10^{-3}	0.514	2.610×10^{-2}	0.934
1/16	289	1/16	3.650×10^{-4}	0.853	2.370×10^{-3}	1.000	2.010×10^{-3}	0.846	1.300×10^{-2}	1.003
1/32	1069	1/32	1.890×10^{-4}	0.949	1.170×10^{-3}	1.014	1.040×10^{-3}	0.944	6.440×10^{-3}	1.014
1/64	4225	1/64	9.350×10^{-5}	1.018	5.500×10^{-4}	1.094	5.220×10^{-4}	1.000	3.270×10^{-3}	0.975

5. REPRESENTATIVE NUMERICAL RESULTS

5.1. Analytical problem and h -convergence study. We first perform an h -convergence study on two-dimensional structured triangular meshes of size h . Consider a unit square to be the computational domain with the following expressions for the saturation and pressure fields:

$$s(x, y, t) = 0.4 + 0.4xy + 0.2 \cos(t + x), \quad (5.1a)$$

$$p(x, y, t) = 2 + x^2y - y^2 + x^2 \sin(y + t) - \frac{1}{3} \cos(t) + \frac{1}{3} \cos(t + 1) - \frac{11}{6}. \quad (5.1b)$$

We replace the source/sink terms (i. e., wells flow rates) of equations (2.1a)–(2.1b) by functions denoted by f_1 and f_2 , obtained via the method of manufactured solutions.. Dirichlet boundary conditions are applied on $\partial\Omega$ on both saturation and pressure fields. The input parameters are:

$$\phi = 2, K = 1, \mu_w = \mu_o = 1, s_{rw} = s_{ro} = 0, k_{rw}(s) = s^2, k_{ro}(s) = (1 - s)^2.$$

The capillary pressure satisfies (2.4) with $\theta = 2$, $p_d = 50$, and $R = 0.05$. Table 1 shows the errors in L^2 and H^1 norms evaluated at $T = 1$ and the corresponding convergence rates for saturation and pressure. The rates are optimal in the H^1 norm. The suboptimal rate in the L^2 norm is expected as first order Taylor expansion is used for capillary pressure, and phase mobilities are evaluated through Picard’s iterations. The vertex scheme results in the theoretical convergence rate of one for both unknowns, which confirms the correct behavior of the algorithm.

5.2. Physical problems. In this section, robustness of the proposed vertex scheme is assessed using standard two- and three-dimensional test problems. Numerical responses of several five spot and quarter-five spot problems, with homogeneous and heterogeneous permeability fields are investigated. We examine the element-wise mass balance property associated with the vertex scheme and also comment on capability of the scheme in satisfying the maximum principle. Let water and oil be the wetting phase and non-wetting phase, respectively. For all problems, the relative permeability and capillary data satisfy (2.3), (2.4) and we assume the following:

$$s_{in} = 0.85, \quad \mu_w = 5 \times 10^{-4} \text{ kg/ms}, \quad \mu_o = 2 \times 10^{-3} \text{ kg/ms}, \quad (5.2)$$

$$\phi = 0.2, \quad p_d = 5 \times 10^3 \text{ Pa}, \quad \theta = 3, \quad s_{rw} = s_{ro} = 0.15, \quad (5.3)$$

$$s^0 = 0.15, \quad p^0 = 1 \times 10^6 \text{ Pa}. \quad (5.4)$$

5.2.1. Two-dimensional homogeneous medium. We take a domain of $\Omega = [0, 100]^2 \text{ m}^2$ with mesh-size of $h = 100/40 \text{ m}$. No-flow boundary condition over $\partial\Omega$ is chosen for this problem (see

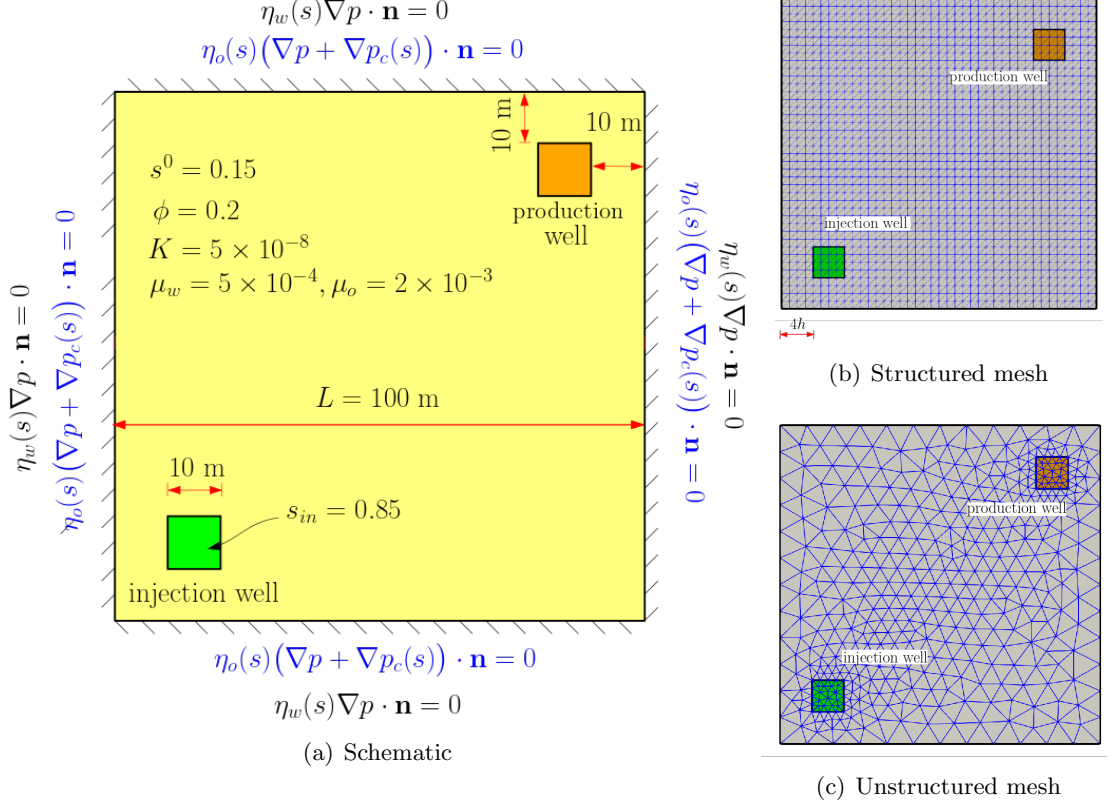


FIGURE 1. Two-dimensional homogeneous medium: This figure provides a pictorial description of the boundary value problem and shows the typical meshes employed in our numerical simulations.

Figure 1(a)) and flow is driven from the injection to the production wells by introducing source and sink terms. The injection and production flow rates satisfy:

$$\int_{\Omega} \bar{q} = \int_{\Omega} \underline{q} = 0.1, \quad (5.5)$$

where \bar{q} is piecewise constant on $[10, 20] \text{ m} \times [10, 20] \text{ m}$ and $\bar{q} = 0$ elsewhere and \underline{q} is piecewise constant on $[80, 90] \text{ m} \times [80, 90] \text{ m}$ and $\underline{q} = 0$ elsewhere. We choose a constant permeability $K = 5 \times 10^{-8} \text{ m}^2$. Domain is discretized with a triangular structured mesh and the time step is $\tau = 60 \text{ s}$. The final simulation time is $T = 12000 \text{ s}$, and we provide solutions snapshots at $t = 1800 \text{ s}$, $t = 6000 \text{ s}$, and $t = 12000 \text{ s}$. The saturation and pressure profiles obtained under vertex scheme are, respectively, displayed in Figures 2(a)–2(c) and 2(d)–2(f). The wetting phase is injected at the lower left end of the domain, and displaces the non-wetting fluid to the upper right corner. Note that this problem is convection-dominated but it is evident that numerical saturation remain within physical bounds ($s_h^n \geq 0.15$ and $s_h^n \leq 0.85$) during simulation and no undershoot and overshoot are observed. It only takes 4 to 5 Picard's iterations at each time step for convergence of the vertex scheme. This is true for all two-dimensional test cases unless specified otherwise.

We compare saturation profiles obtained from the vertex scheme with the solutions obtained from the fully implicit discontinuous Galerkin (DG) formulation developed by Epshteyn and Riviere [2007]. For the chosen DG formulation polynomial order is set to $\mathbb{P} = 1$, DG symmetry parameter is set to $\epsilon = +1$ (i.e., NIPG), and the penalty parameter is set to $\sigma = 0.1$. Both DG formulation

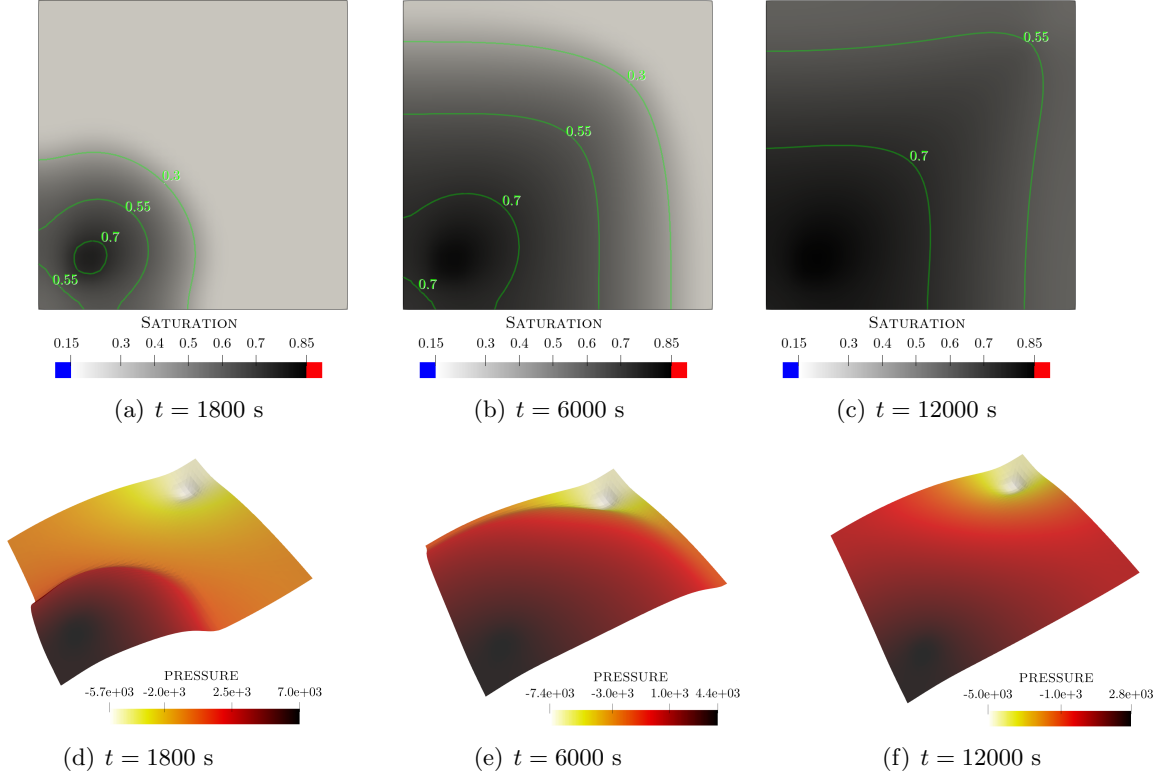


FIGURE 2. Two-dimensional homogeneous medium: This figure shows the saturation and pressure profiles obtained from the proposed vertex scheme at three different time steps. Structured triangular mesh is used (see Figure 1(b)). The saturation field (top figures) should be between 0.15 and 0.85. This figure suggests that the proposed scheme is capable of providing maximum-principle satisfying results. To wit, no undershoots (blue-color cell) or overshoots (red-colored cell) observed. Highest value and lowest value of pressure solutions (bottom figures) detected at the injection well and the production well, respectively. The pressure difference forces the wetting phase flow through the domain. Pressure differences subside as the front reaches the production well. Pressure solutions are warped for better visualization.

and vertex scheme are solved on the structured triangular mesh (as shown in Figure 1(b)) and the time step is $\tau = 60$ s.

For three representative time steps, the saturation and pressure profiles, along the diagonal $\{(x, y) : x = y\}$ from the injection well upto production well are illustrated in Figures 3(a) and 3(b). We observe that the finite element solutions are accurate and in very good agreement with the DG solutions. It can be seen that the saturation fronts, under both DG and proposed vertex scheme, propagates with the same speed. We recall that the proposed finite element scheme satisfies a maximum principle, as mentioned in Proposition 3.1. However, the DG approximations of the saturation are not guaranteed to satisfy (3.5) and small undershoot (usually at the injection well) and overshoots (usually right after the saturation front) are observed for saturation profile. Increasing DG polynomial order (in addition to sharpening front) is reported to relatively reduce

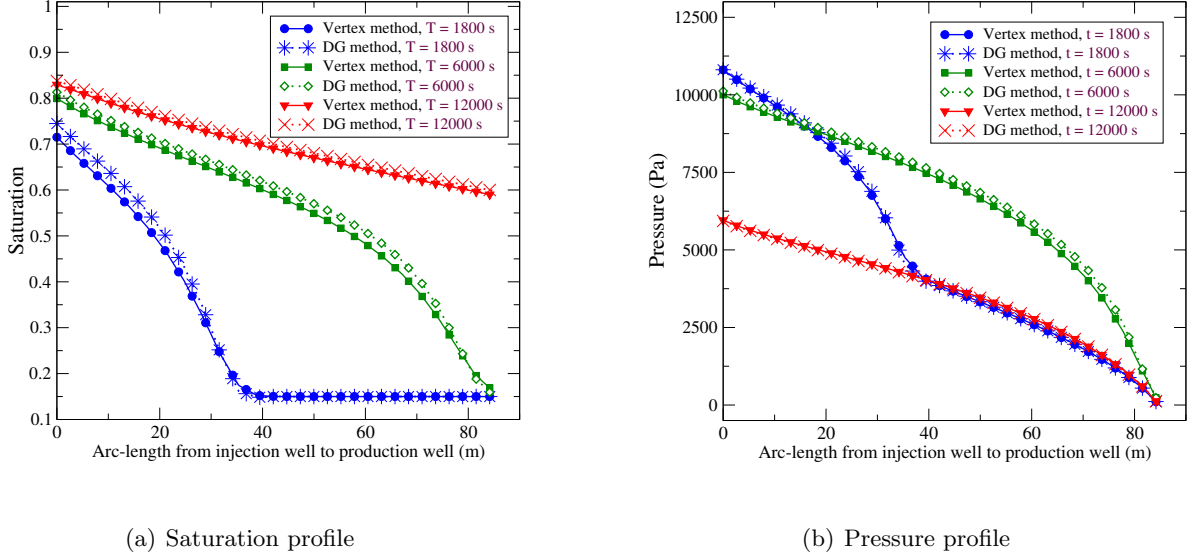


FIGURE 3. Two-dimensional homogeneous medium: This figure compares the saturation and pressure profiles obtained from the vertex scheme and a first order discontinuous Galerkin formulation (i.e., DG-NIPG with $\mathbb{P} = 1$ and $\sigma = 0.1$). Solutions are plotted along the diagonal line spanned from point (20, 20) m to point (80, 80) m. DG and vertex scheme reproduce similar responses throughout the simulation. Given that our solutions are only plotted on the diagonal line, the results from the left figure should be treated with considerable caution. As highlighted in Figure 2, saturation solutions under the vertex scheme are always bounded by physical values. However, we are aware the DG method (and finite element methods in general) do not enjoy maximum principle. For example, in this experiment the lowest and highest value of saturation found under the DG-NIPG formulation was 0.148 and 1.185, respectively.

these unphysical violations [Epshteyn and Riviere, 2009]. Even so, DG schemes still require external bound-preserving mechanisms such as slope/flux limiting [Kuzmin, 2010], artificial viscosity [der Ven and der Vegt, 2002], or nodal-based optimization [Joshaghani and Nakshatrala, 2020] to completely enforce maximum principle. A comprehensive survey of bound-preserving methods is described in [Zhang and Shu, 2011].

5.2.2. *Conservation of local mass balance.* Next, we investigate the local mass conservation property of the proposed scheme for the incompressible two-phase flow model. The local mass conservation of an element ω at each time step, is calculated as follows:

$$m(E) = \int_E \frac{\phi(s_h^n - s_h^{n-1})}{\tau} - \int_{\partial E} \eta_w(s^n) K_E \nabla p^n \cdot \mathbf{n}_E - \int_E (f_w(s_{\text{in}}) \bar{q} + f_w(s^n) \underline{q}). \quad (5.6)$$

A true locally mass conservative scheme should produce the zero value for $m(E)$ for each element E . We compute the mass balance values for the problem described in Section 5.2.1. In Figure 4, the values of $m(E)$ are displayed at three representative time steps. One can see that the magnitude of

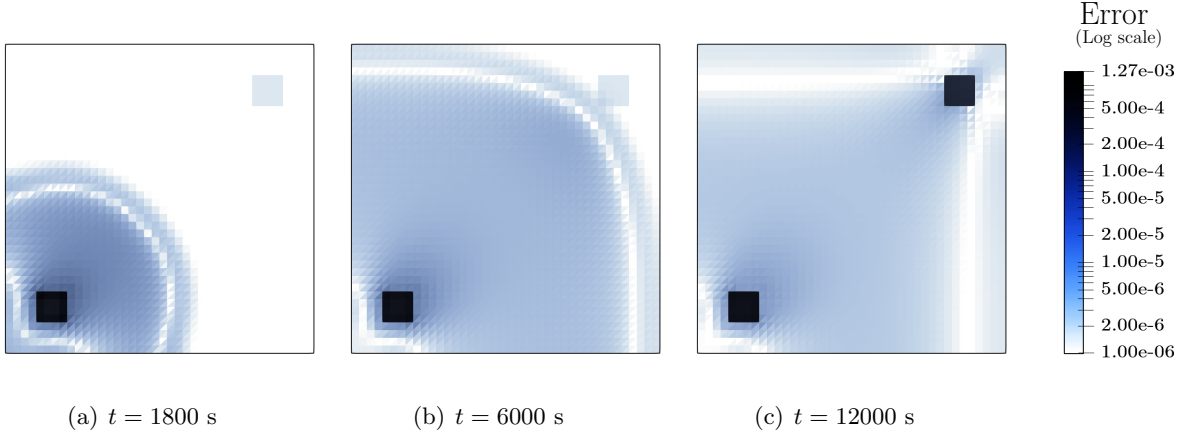


FIGURE 4. Local mass balance conservation: This figure illustrates the local mass conservation properties of the vertex scheme for two-phase incompressible flow problem on a homogeneous domain. The mass balance error remains small as time advances. This value is always less than 10^{-5} inside the reservoir (excluding elements allocated to wells).

$m(E)$ in the domain (except at the wells' locations) is always less than 10^{-5} , which is the tolerance set for the Picard's iteration. Hence, the proposed scheme is locally mass conservative. We note that the source/sink models result in a higher mass balance error values (of the order of 10^{-3}) on the elements that form the support of the injection and production wells.

5.2.3. *Two-dimensional domain with unstructured mesh.* All parameters are the same as in Section 5.2.1, except for the mesh that is triangular unstructured as depicted in Figure 1(c). Figure 5 shows the saturation profiles at four different time steps. We observe that the saturation remains bounded and no violations of maximum principle are observed throughout the simulation. This result also shows that the proposed finite element scheme handles unstructured meshes as expected.

5.2.4. *Two-dimensional porous media with low permeability block.* In this problem, the domain is $\Omega = [0, 100]^2$ m², and as shown in Figure 6 the permeability is 5×10^{-8} everywhere except inside the square inclusion of size $L = 20$ m, where the permeability k_{In} is 10 times smaller. The remaining parameters are the same as in Section 5.2.1. The saturation solutions at different time steps are depicted in Figure 7. As expected, the wetting phase initially avoids the region of lower permeability, while still traveling towards the production well. Toward the end of the simulation, we can observe that the wetting phase has started to penetrate the inclusion region. However, when we increase order of difference in permeabilities (e.g., $K/K_{\text{In}} = 10000$), the inclusion becomes impenetrable throughout the simulation. This trend is clearly shown in Figure 8 and was reported in the literature for single-phase flow [Li and Riviere, 2015], and two-phase flow [Fabien et al., 2020]. Figures 7 and 8 also highlight that the vertex scheme (on a relatively coarse mesh) is capable of generating sharp saturation front in the domain with non-homogeneous permeability, in addition to completely suppressing undershoots and overshoots in the saturation profile. Snapshots of the pressure solution along the diagonal line are shown in Figure 9. The less permeable region slightly undulates the curve in that region by increasing the pressure drop. However, similar to results obtained in homogeneous porous media (see Figure 3(b)), the pressure difference drops as more wetting phase reaches the production well.

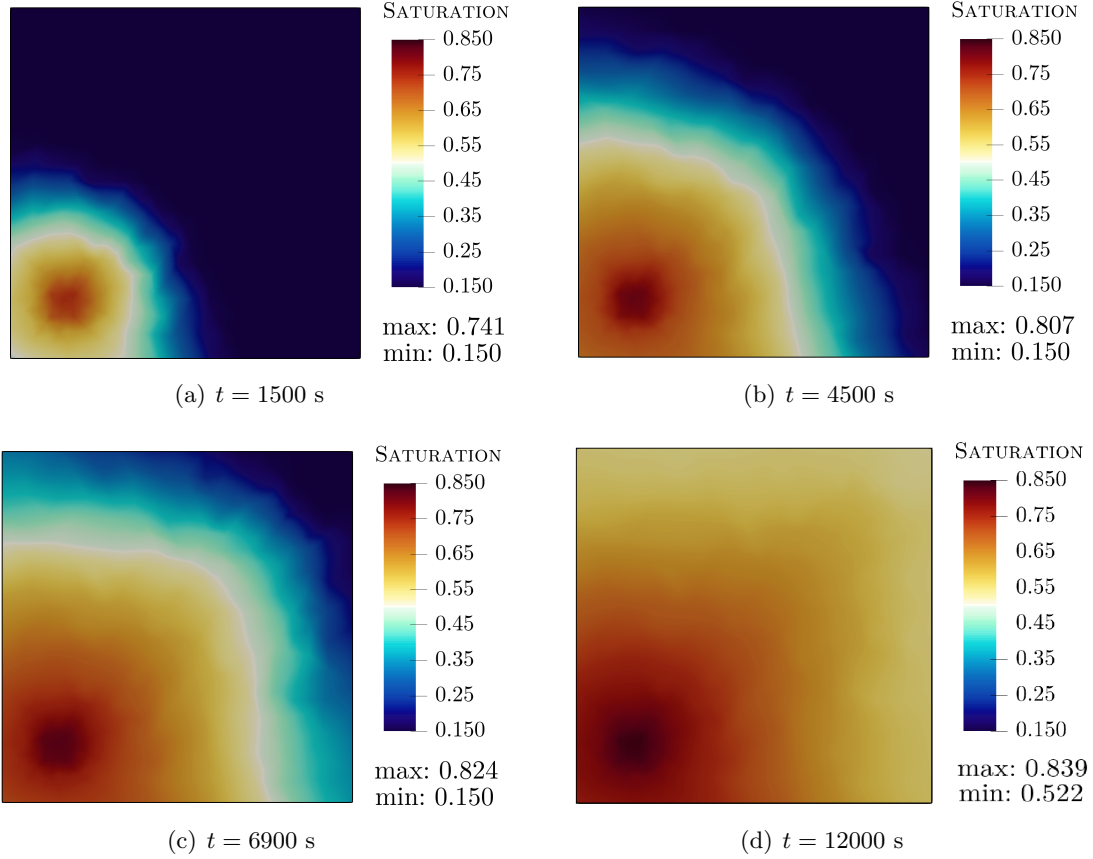


FIGURE 5. Two-dimensional homogeneous domain with unstructured mesh: This figure shows saturation contour plots obtained on an unstructured triangular mesh (Figure 1(c)). These results pinpoint that the proposed scheme can provide accurate and maximum-principle satisfying results on unstructured meshes.

5.2.5. *Two-dimensional porous medium with highly heterogeneous permeability.* In this example, the domain $\Omega = [0, 1000]^2$ m² is highly heterogeneous because the permeability field is taken from various horizontal permeability slices from model 2 of the SPE10 benchmark model [Christie et al., 2001; SPE]. This model is characterized by two formations: a shallow-marine Tarbert formation in the top 35 layers, where the permeability field is relatively smooth, and a fluivial Upper-Ness permeability in the bottom 50 layers. Both formations are characterized by large permeability variations, 8–12 orders of magnitude, but are qualitatively different. We choose layer 1 from Tarbert formation and layer 45 and 80 from Upper-Ness formation. Figure 10(a), 10(b), and 10(c) show the selected permeability layers. These permeability slices are scaled to a 60×60 grid, instead of the original 60×220 grid. The porosity is set to 0.2. No flow boundary conditions are prescribed on the entire boundary and as shown in Figure 11 an injection well of size 100×100 m is defined on the center of domain and four production wells with size of 100×100 m are located near the corners of the domain. Injection and production flow rates are piecewise constant with compact

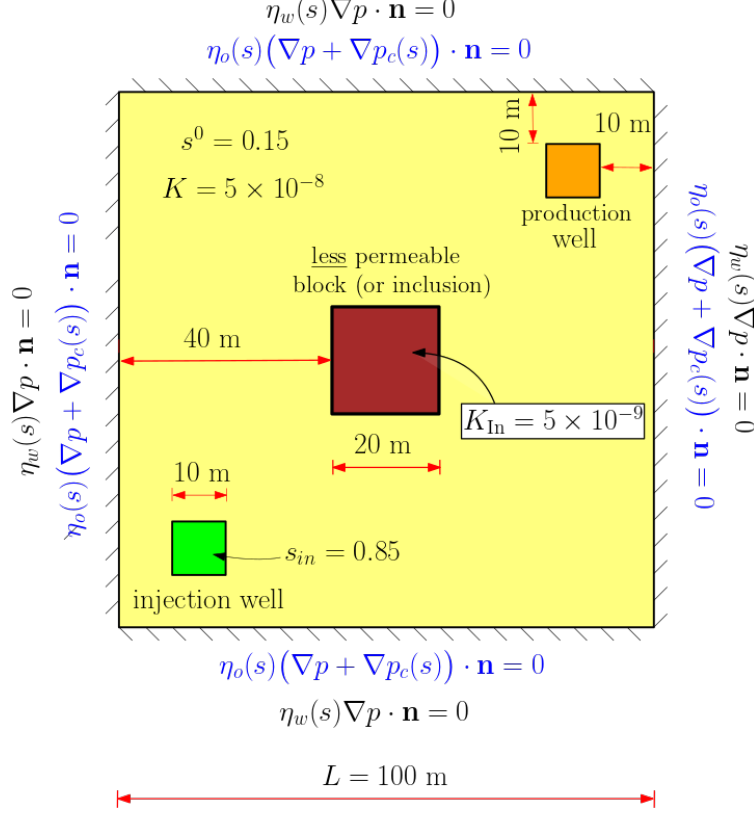


FIGURE 6. Two-dimensional porous media with low permeability block: This figure shows the representative computational domain and the boundary value problem. No flow boundary conditions are assigned along all boundaries.

support and are determined by the following constraint:

$$\int_{\Omega} \bar{q} = \int_{\Omega} \underline{q} = 2.8 \times 10^{-1}. \quad (5.7)$$

Here we employ the proposed finite element scheme on a structured mesh with 7200 triangular elements. The simulation runs to $T = 2.5$ days with 600 time steps, and we provide the solutions at $t = 0.4125$, $t = 0.725$, and 2.5 days. Saturation contours are depicted in Figure 12. The wetting phase moves from the injection wells towards the four production wells as expected. The permeability field determines the pattern of the saturation front throughout the porous media. For all three cases, physical instabilities in form of separate finger-like intrusions are generated. As expected, the saturation front forms a curve that is less smooth for porous media of Upper Ness types (i.e., layers 45 and 80). It is evident that the vertex scheme produces bound-preserving saturations and that fronts avoid small regions of lower permeability.

5.2.6. Three-dimensional porous medium. Herein we validate our vertex scheme in a three-dimensional set-up. In particular, we investigate an extension of the numerical experiment performed in Section 5.2.1. The domain is $\Omega = [0, 1000]^3$ m³ and is partitioned into an unstructured mesh of tetrahedron elements, as shown in Figure 13(b). The permeability is fixed to $K = 5 \times 10^{-8}$ m². No flow boundary condition is employed on the entire boundary $\partial\Omega$. Production and injection wells of size (10, 10, 10) m with constant flow rates of $\bar{q} = \underline{q} = 0.001$ are

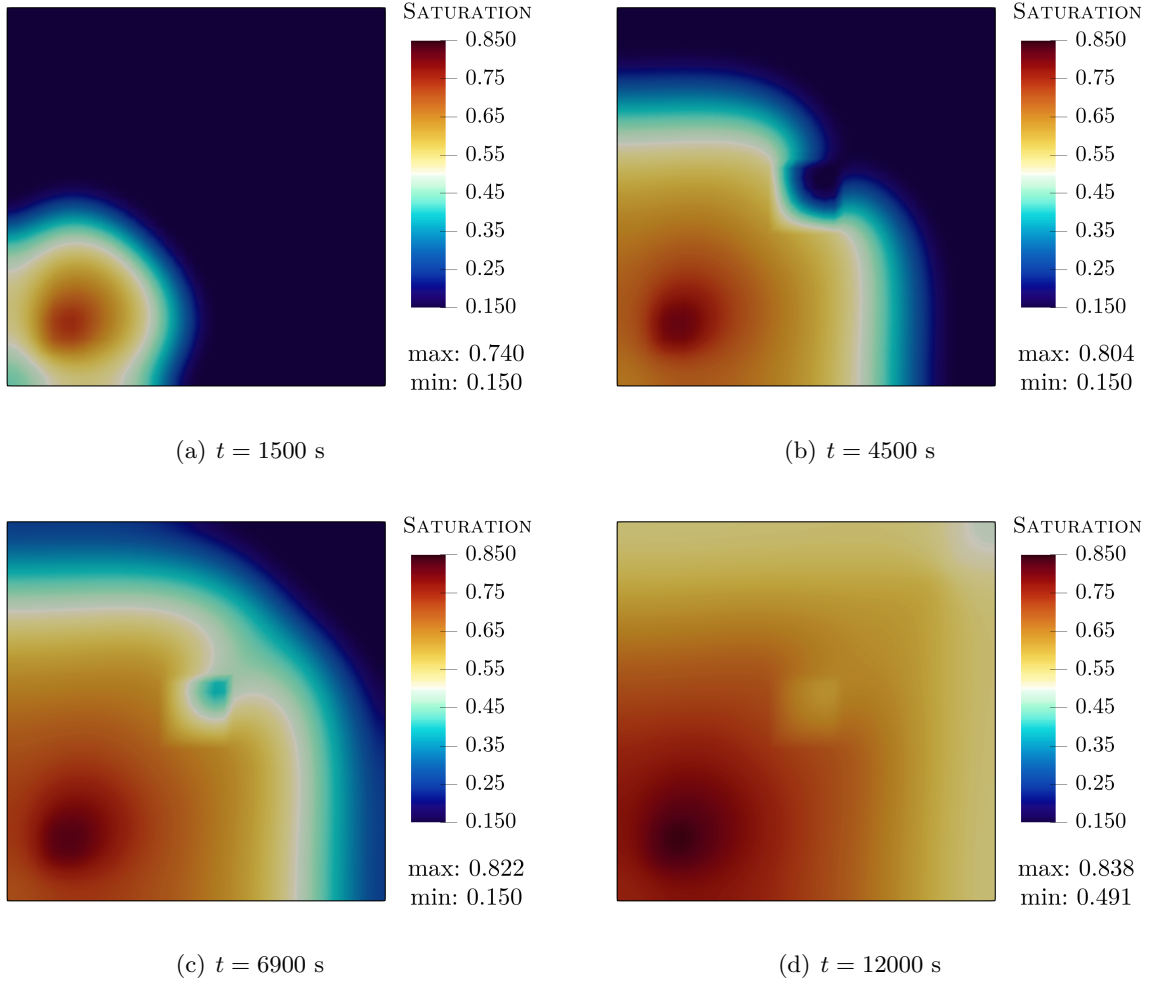


FIGURE 7. Two-dimensional medium with a low permeability block: This figure shows the evolution of saturation solutions. Permeability of block is one order of magnitude smaller than the rest of domain. Structured triangular mesh (Figure 1(c)) was used for this problem. Vertex scheme exhibits the expected response, since the saturation avoids the region of low permeability. We note that no violations with respect to maximum principle occurred and saturation field remains smooth and monotone even near the corners of the low permeability block.

positioned at the opposite corners of the domain. Figure 13(a) shows the computational domain and the boundary conditions for this problem. The final time is set to $T = 2$ days and the time step is set to $\tau = 216$ s. In Figure 14, snapshots of the wetting phase saturation are given at times $t = 0.125$, $t = 0.5$, $t = 1$, and $t = 2$ days. Profile of pressure at the corresponding time steps, along the diagonal (from injection well to production well), are exhibited in Figure 15. One can observe that the numerical scheme is robust in three-dimensional domain and the resulting saturation satisfies the maximum principle. Only 5 to 6 Picard's iterations are needed at each time step for convergence of the vertex scheme. This is true for all three-dimensional test cases.

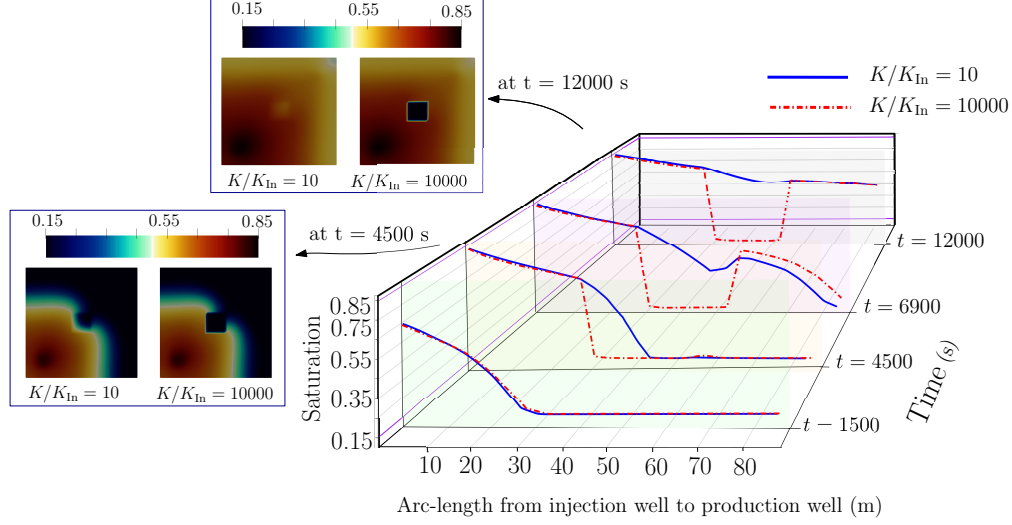


FIGURE 8. Two-dimensional medium with a low permeability block: This figure shows evolution of the saturation profile along the diagonal line and compares the solutions for two cases: (i) domain with a less permeable block (i.e., $K/K_{In} = 10$) and (ii) domain with almost impermeable block (i.e., $K/K_{In} = 10000$). In first case, fluid initially evades the block but as time progresses saturation inside the block starts to increase. However, for the second case, higher permeability difference has made the inclusion impenetrable throughout the simulation. We observe that vertex scheme delivers satisfactory results with respect to maximum principle.

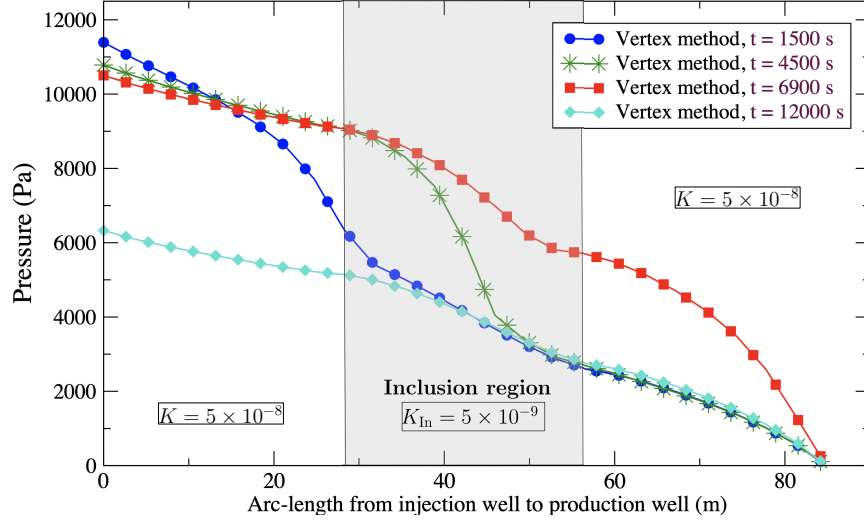


FIGURE 9. Two-dimensional medium with a low permeability block: This figure shows the evolution of the numerical pressure. Profiles are plotted along the diagonal line from point (20, 20) m to (80, 80) m. The pressure values drop as we move from the injection well toward the production well. The inclusion (or the block) region, which is illustrated with gray-color, slightly perturbs the solutions.

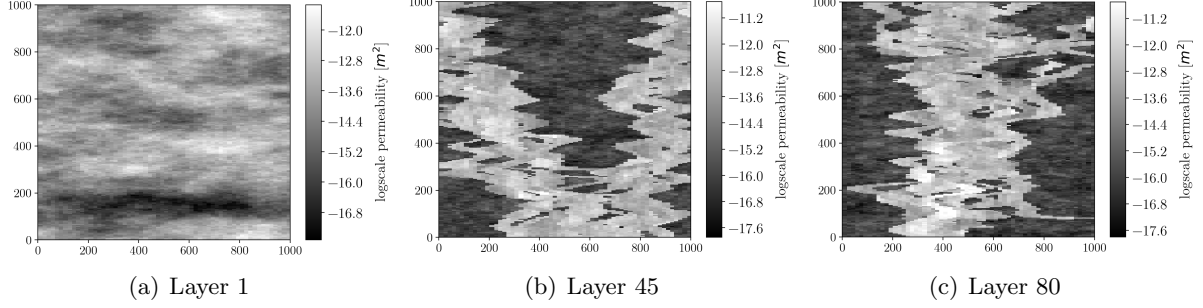


FIGURE 10. Two-dimensional porous medium with highly heterogeneous permeability: This figure depicts the permeability fields adopted from three horizontal layers of SPE10 benchmark model. Each field is scaled to a resolution of 60×60 grids. Layer 1 taken from relatively smooth Tarbert formation, while layer 45 and 80 are taken from more rugged Upper-Ness formation. Values are displayed in logarithmic scale, since they vary across a wide range.

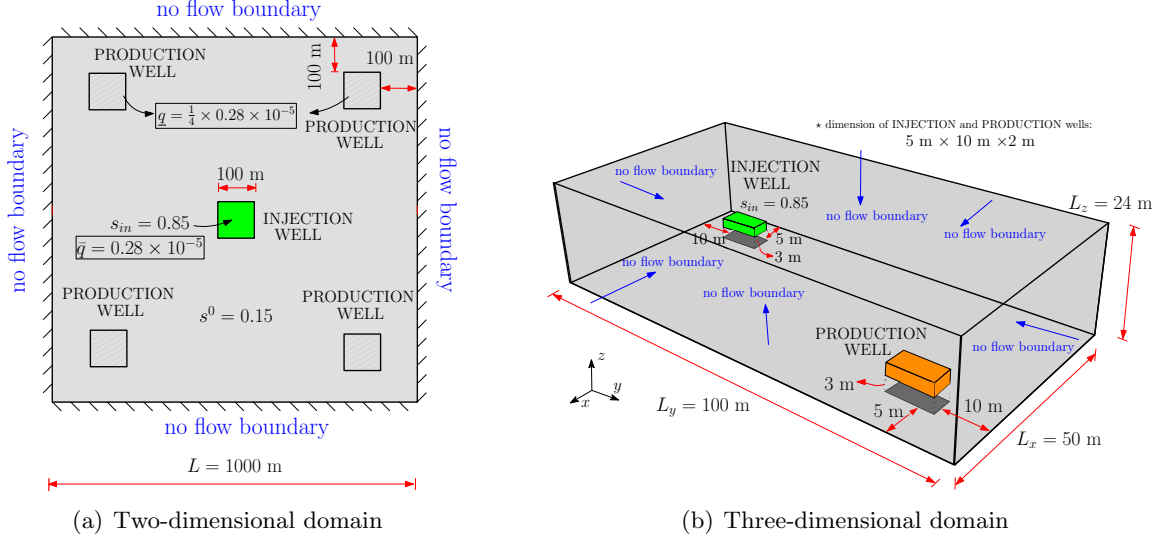


FIGURE 11. Highly heterogeneous problems: This figure provides a pictorial description of the boundary value problem and shows the computational domain used in numerical simulations. For both two-dimensional and three-dimensional problems no flow conditions are assigned across all boundaries. Fluid flow is hence driven by the pressure difference prompted by injection and production wells.

5.2.7. *Three-dimensional porous medium with highly heterogeneous permeability.* In realistic problems, heterogeneities in three-dimensional media have a large impact on the propagation of the fluid phases. We now examine a three-dimensional problem analogous to the 2D numerical experiment carried out in Section 5.2.6. The aim of this boundary value problem is to show that the proposed finite element method can perform satisfactorily in highly heterogeneous three-dimensional domains. The domain is $\Omega = [0, 50] \times [0, 100] \times [0, 24] \text{ m}^3$. As shown in Figure 16, we

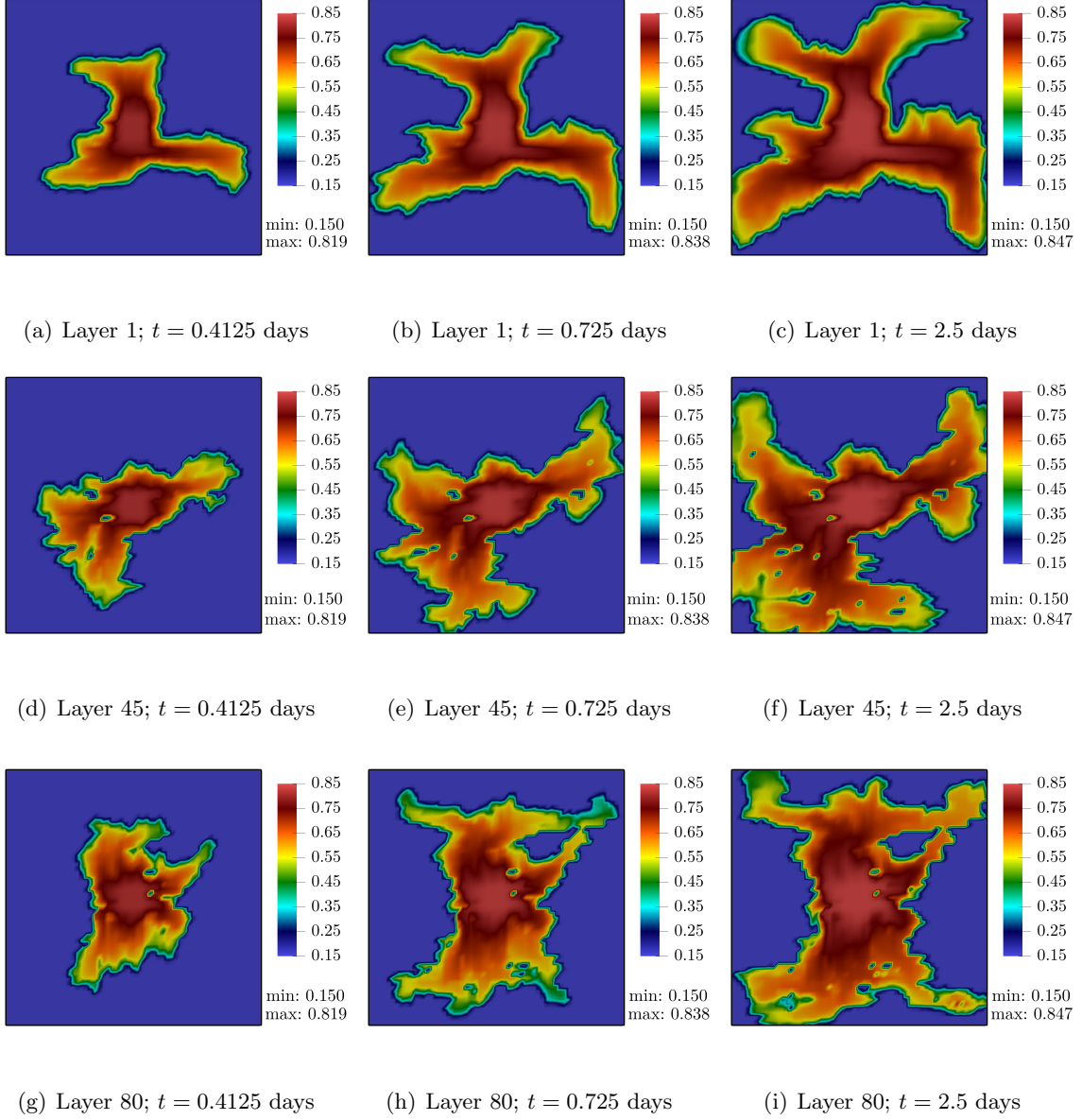


FIGURE 12. Two-dimensional heterogeneous problem: This figure shows the evolution of the wetting phase saturation for the three chosen layers. For all cases, permeability field determines the pattern fluid flows through porous media. Layer 1 (top figures), compared to other layers, leads to smoother saturation front boundaries. This observation is justified as the permeability field associated with layer 1 is not as highly varying as for the other layers. This figure also reiterates that the vertex scheme always produces physical values of saturations, without any overshoots and undershoots, even for domains with permeabilities that vary over many orders of magnitudes.

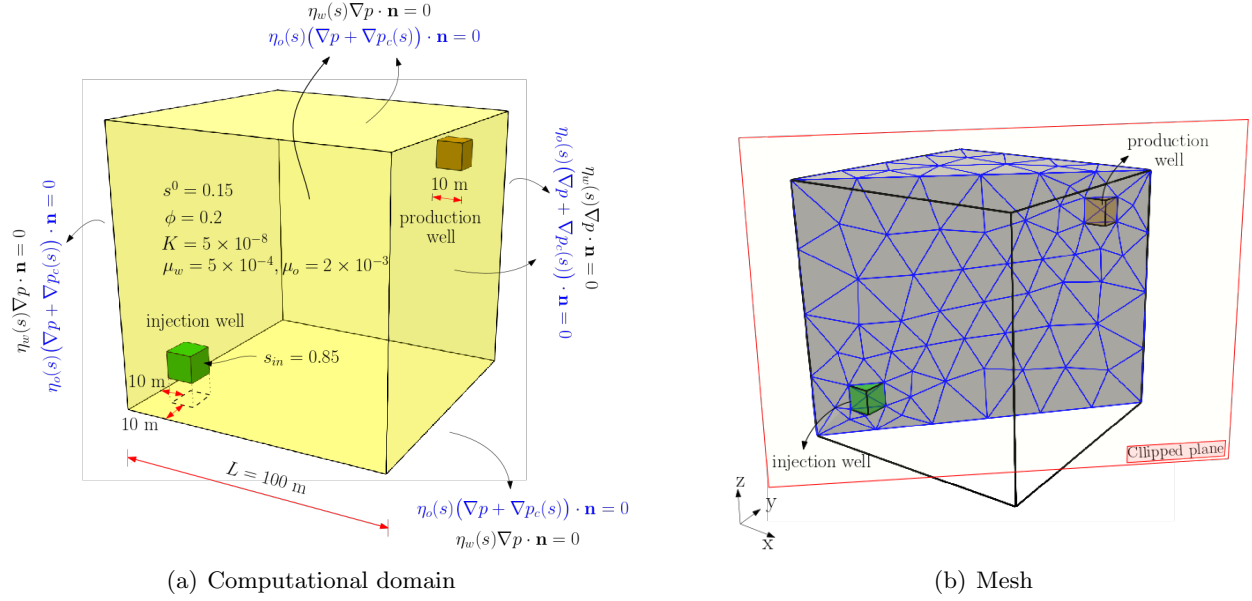


FIGURE 13. Three-dimensional porous medium with homogeneous permeability Left figure provides a pictorial description of the boundary value problem. no flow conditions prescribed on all boundaries. Right figure shows a cross-sectional view of the mesh applied in our numerical experiment.

adopt a sample permeability field of size $32 \text{ m} \times 64 \text{ m} \times 12 \text{ m}$ from the SPE10 benchmark problem [SPE]. The coordinates of injection and production wells are $(7.5, 15, 4) \text{ m}$ and $(42.5, 85, 4) \text{ m}$, respectively (see Figure 11(b)). The size of both wells are $5 \text{ m} \times 10 \text{ m} \times 2 \text{ m}$ with $\int_{\Omega} \bar{q} = \int_{\Omega} \underline{q} = 0.1$. The mesh is made of 19200 structured tetrahedral elements. Total time is set to $T = 3$ days and the time step is $\tau = 259.2 \text{ s}$. We apply the proposed finite element method and plot the saturation contours at different time steps in Figure 17. The wetting phase reaches the production well by sweeping the regions with highest permeability value. Evidently, the numerical saturation remains within physical bounds and no undershoots and overshoots are observed. This experiments reinforces that the proposed scheme satisfies the maximum-principle for two-phase incompressible flow and remains robust for highly heterogeneous three-dimensional media.

6. CONCLUSION

We have developed a new first-order finite element method with mass-lumping and flux upwinding, which we refer to as vertex scheme, to solve the immiscible two-phase flow problem in porous media. We show optimal convergence rates for manufactured solutions. Numerical examples in two and three dimensions pinpoint that the method is accurate, and robust, even in the case of realistic discontinuous highly varying permeability. Furthermore, we show that the proposed method is locally mass-conservative and the resulting solutions satisfy the maximum principle. The method is mesh-independent and does not require penalization or any external bound-preserving mechanism.

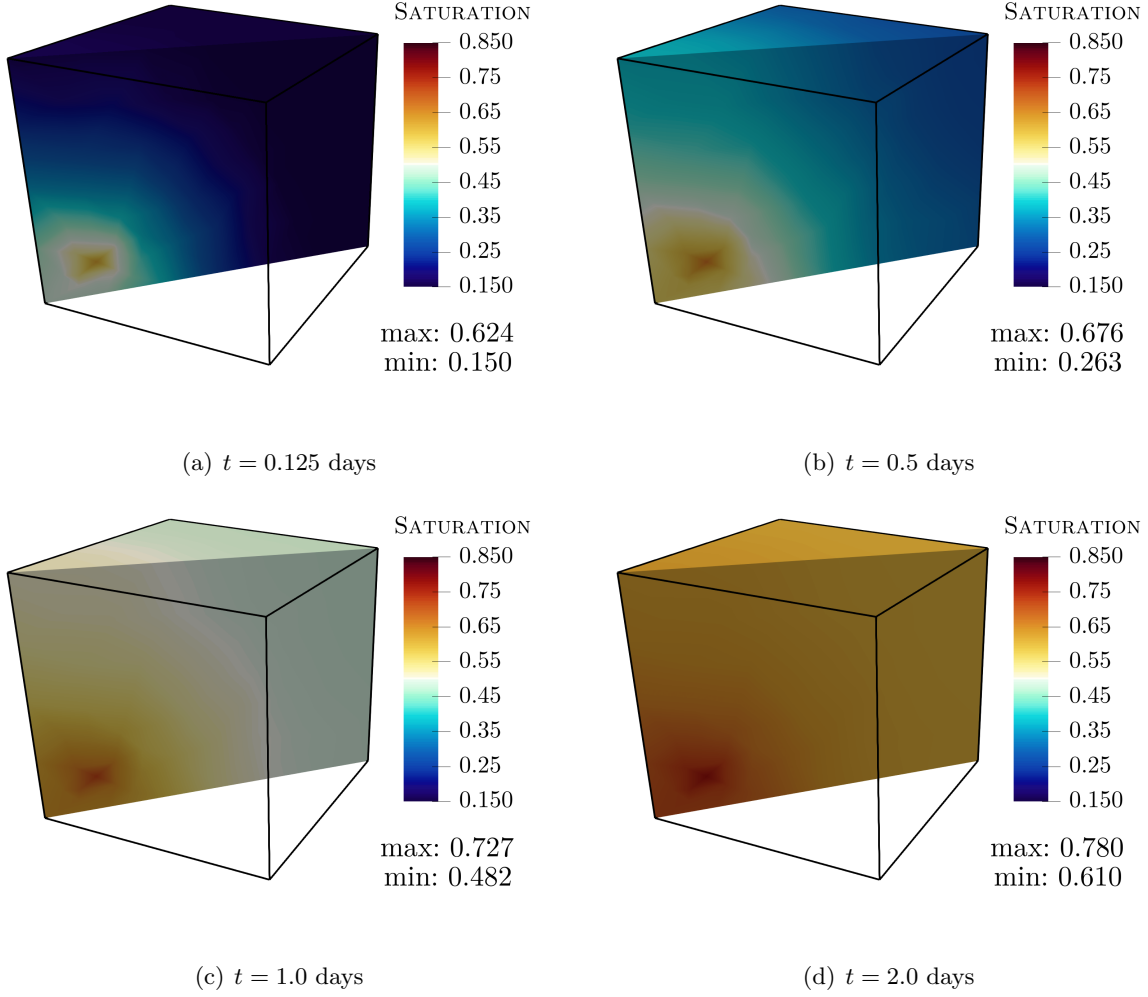


FIGURE 14. Three-dimensional porous medium: This figure shows saturation contours in a homogeneous domain with $K = 5 \times 10^{-8} \text{ m}^2$. Unstructured tetrahedron mesh (Figure 13(b)) is used for this experiment. Similar to two-dimensional problems, the scheme exhibits satisfactory results with respect to maximum principle. This means that solutions always remain between 0.15 and 0.85. In this figure a cutaway view of solutions is provided for better visualization.

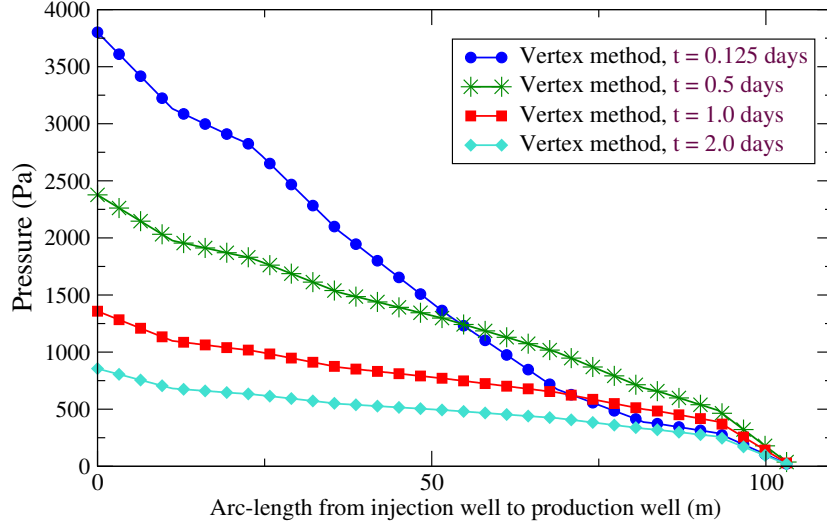


FIGURE 15. Three-dimensional porous medium: This figure shows pressure solutions obtained from the vertex scheme on a homogeneous domain with $K = 5 \times 10^{-8} \text{ m}^2$. Profiles are plotted on the diagonal line from point (20, 20, 20) m to point (80, 80, 80) m. Vertex scheme correctly predicts the response. Maximum and minimum pressures are detected on the injection well and production well, respectively. As time advances, more fluid reaches the production well and the pressure difference decreases.

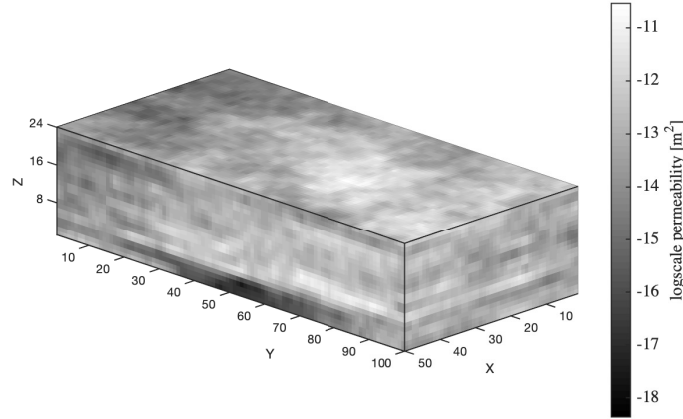


FIGURE 16. Three-dimensional porous medium with highly heterogeneous permeability: This figure shows the permeability field extracted from SPE10 benchmark model. The resolution of this field is $32 \times 64 \times 12$ grids. Values are displayed in logarithmic scale, since they vary across a wide range.

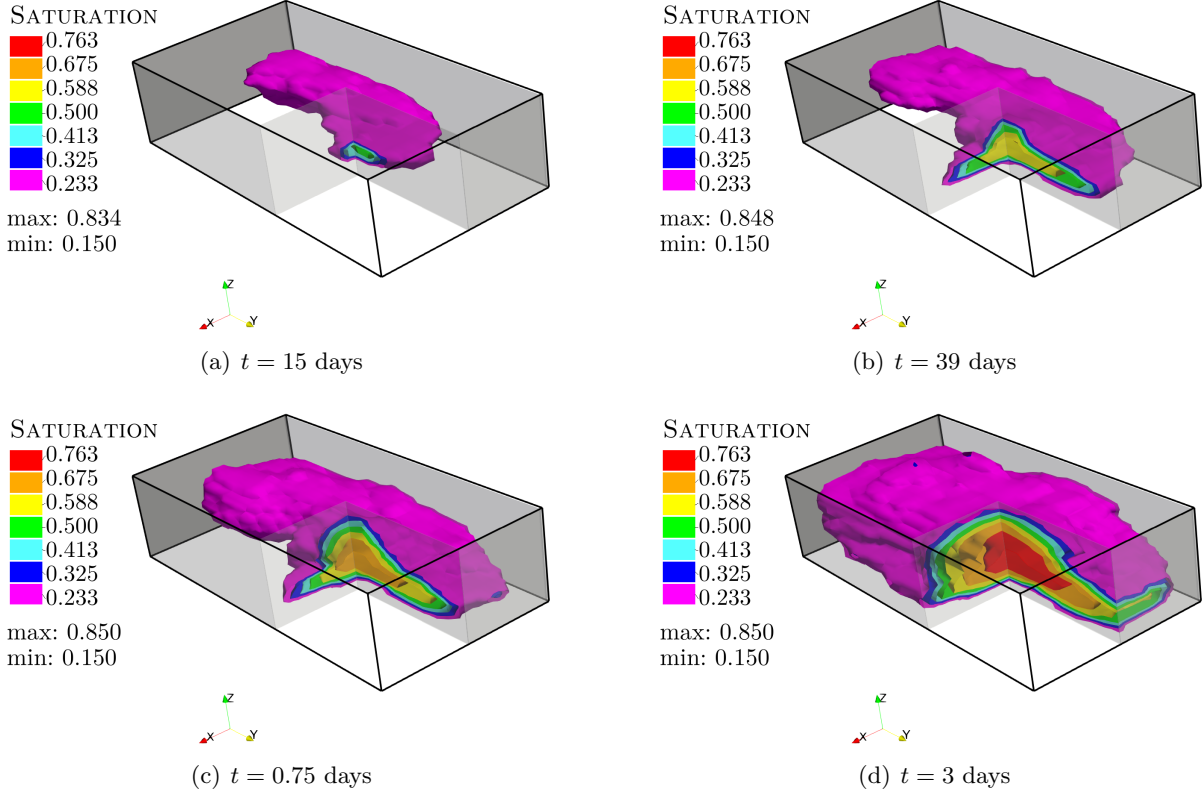


FIGURE 17. Three-dimensional SPE10 problem: This figure shows contours of the saturation solutions obtained under the proposed vertex scheme on a highly heterogeneous domain (i.e., SPE10 permeability field). The numerical experiment performed on a structured tetrahedron mesh with 19200 elements. The main inference from this figure is that (i) the proposed scheme generates robust and accurate results. It can be seen that the wetting phase fluid flows through the most permeable pore-networks from injection well towards production well. (ii) The scheme always respects maximum principle, since no undershoots and overshoots has been detected throughout the simulation. (For interpretation of the references to color in this figure legend, the reader is referred to the web version of this article.)

APPENDIX

Below, we have provided the PETSc command-line options for the Schur complement approach discussed in Section 4. (see online version for color-coded terms).

LISTING 1. PETSc command-line options for the proposed Schur complement approach

```
# Outer solver
PETScOptions.set("ksp_type", "fgmres")
PETScOptions.set("ksp_rtol", 1e-8)

# Schur complement with full factorization
PETScOptions.set('pc_type', 'fieldsplit')
PETScOptions.set('pc_fieldsplit_type', 'schur')
PETScOptions.set('pc_fieldsplit_schur_fact_type', 'full')

# Diagonal mass lumping
PETScOptions.set('pc_fieldsplit_schur_precondition', 'selfp')

# Automatically determine fields based on zero diagonal entries
PETScOptions.set('pc_fieldsplit_detect_saddle_point')

# Single sweep of ILU(0) for the mass matrix
PETScOptions.set('fieldsplit_0_ksp_type', 'preonly')
PETScOptions.set('fieldsplit_0_pc_type', 'ilu')

# Single sweep of multi-grid for the Schur complement
PETScOptions.set('fieldsplit_1_ksp_type', 'preonly')
PETScOptions.set('fieldsplit_1_pc_type', 'hypre')
```

References

- SPE comparative solution project model 2. <http://www.spe.org/web/csp/datasets/set02.htm>. Accessed:2019-07-10.
- L. M. Abriola and K. Rathfelder. Mass balance errors in modeling two-phase immiscible flows: causes and remedies. *Advances in Water resources*, 16(4):223–239, 1993.
- S. Balay, S. Abhyankar, M. F. Adams, J. Brown, P. Brune, K. Buschelman, L. Dalcin, V. Eijkhout, W. D. Gropp, D. Kaushik, M. G. Knepley, L. C. McInnes, K. Rupp, B. F. Smith, S. Zampini, H. Zhang, and H. Zhang. PETSc users manual. Technical Report ANL-95/11 - Revision 3.8, Argonne National Laboratory, 2017.
- S. Balay, S. Abhyankar, M. F. Adams, J. Brown, P. Brune, K. Buschelman, L. Dalcin, V. Eijkhout, W. D. Gropp, D. Kaushik, M. G. Knepley, D. A. May, L. C. McInnes, R. T. Mills, T. Munson, K. Rupp, P. Sanan, B. F. Smith, S. Zampini, H. Zhang, and H. Zhang. PETSc Web page, 2018.
- R. Brooks and T. Corey. Hydraulic properties of porous media. *Hydrology Papers, Colorado State University*, 24:37, 1964.
- J. Brown, M. G. Knepley, D. A. May, L. C. McInnes, and B. Smith. Composable linear solvers for multiphysics. In *Parallel and Distributed Computing (ISPDC), 2012 11th International Symposium on*, pages 55–62. IEEE, 2012.

- G. Chavent and J. Jaffré. *Mathematical Models and Finite Elements for Reservoir Simulation: Single-Phase, Multiphase and Multicomponent Flows Through Porous Media*. Elsevier, 1986.
- C. M. Chen and V. Thomée. The lumped mass finite element method for a parabolic problem. *The ANZIAM Journal*, 26(3):329–354, 1985.
- Z. Chen and R. E. Ewing. Degenerate two-phase incompressible flow III. sharp error estimates. *Numerische Mathematik*, 90(2):215–240, 2001.
- M. Christie, M. Andrew, and M. J. Blunt. Tenth spe comparative solution project: A comparison of upscaling techniques. In *SPE Reservoir Simulation Symposium*. Society of Petroleum Engineers, 2001.
- G. Cohen, P. Joly, J. E. Roberts, and N. Tordjman. Higher order triangular finite elements with mass lumping for the wave equation. *SIAM Journal on Numerical Analysis*, 38(6):2047–2078, 2001.
- L. D. Dalcin, R. R. Paz, P. A. Kler, and A. Cosimo. Parallel distributed computing using Python. *Advances in Water Resources*, 34(9):1124–1139, 2011.
- H. Van der Ven and J. W. Van der Vegt. Space–time discontinuous Galerkin finite element method with dynamic grid motion for inviscid compressible flows: II. efficient flux quadrature. *Computer Methods in Applied Mechanics and Engineering*, 191(41–42):4747–4780, 2002.
- J. Douglas. Finite difference methods for two-phase incompressible flow in porous media. *SIAM Journal on Numerical Analysis*, 20(4):681–696, 1983.
- Y. Epshteyn and B. Riviere. Fully implicit discontinuous finite element methods for two-phase flow. *Applied Numerical Mathematics*, 57(4):383–401, 2007.
- Y. Epshteyn and B. Riviere. Analysis of hp discontinuous galerkin methods for incompressible two-phase flow. *Journal of Computational and Applied Mathematics*, 225(2):487–509, 2009.
- R. Eymard, R. Herbin, and A. Michel. Mathematical study of a petroleum-engineering scheme. *ESAIM: Mathematical Modelling and Numerical Analysis*, 37(6):937–972, 2003.
- R. Eymard, C. Guichard, R. Herbin, and R. Masson. Gradient schemes for two-phase flow in heterogeneous porous media and Richards equation. *Journal of Applied Mathematics and Mechanics/Zeitschrift für Angewandte Mathematik und Mechanik*, 94(7–8):560–585, 2014.
- M. S. Fabien, M. Knepley, and B. Riviere. A high order hybridizable discontinuous galerkin method for incompressible miscible displacement in heterogeneous media. *Results in Applied Mathematics*, page 100089, 2020.
- R. D. Falgout and U. M. Yang. HYPRE: A library of high performance preconditioners. In *International Conference on Computational Science*, pages 632–641. Springer, 2002.
- P. A. Forsyth. A control volume finite element approach to NAPL groundwater contamination. *SIAM Journal on Scientific and Statistical Computing*, 12:1029–1057, 1991.
- M. T. Van Genuchten. A closed-form equation for predicting the hydraulic conductivity of unsaturated soils. *Soil science society of America journal*, 44(5):892–898, 1980.
- V. Girault, B. Riviere, and L. Capanera. A finite element method for degenerate two-phase flow in porous media. part i: Well-posedness. *Journal of Numerical Mathematics*, 2020a.
- V. Girault, B. Riviere, and L. Capanera. A finite element method for degenerate two-phase flow in porous media. part ii: Convergence. *Journal of Numerical Mathematics*, 2020b.
- M. S. Joshaghani and K. B. Nakshatrala. A modeling framework for coupling plasticity with species diffusion. *arXiv preprint arXiv:2011.06652*, 2020.

- M. S. Joshaghani, J. Chang, K. B. Nakshatrala, and M. G. Knepley. Composable block solvers for the four-field double porosity/permeability model. *Journal of Computational Physics*, 386:428–466, 2019.
- D. Kuzmin. A vertex-based hierarchical slope limiter for p-adaptive discontinuous galerkin methods. *Journal of Computational and Applied Mathematics*, 233(12):3077–3085, 2010.
- J. Li and B. Riviere. Numerical solutions of the incompressible miscible displacement equations in heterogeneous media. *Computer Methods in Applied Mechanics and Engineering*, 292:107–121, 2015.
- A. Logg and G. N. Wells. Dofin: Automated finite element computing. *ACM Transactions on Mathematical Software*, 37(2), 2010. doi: 10.1145/1731022.1731030.
- A. Logg, G. N. Wells, and J. Hake. *DOLFIN: a C++/Python Finite Element Library*, chapter 10. Springer, 2012.
- N. K. Mapakshi, J. Chang, and K. B. Nakshatrala. A scalable variational inequality approach for flow through porous media models with pressure-dependent viscosity. *Journal of Computational Physics*, 359:137–163, 2018.
- A. Michel. A finite volume scheme for the simulation of two-phase incompressible flow in porous media. *SIAM Journal of Numerical Analysis*, 41:1301–1317, 2003.
- M. Ohlberger. Convergence of a mixed finite element - finite volume method for the two phase flow in porous media. *East-West Journal of Numerical Mathematics*, 5:183–210, 1997.
- Y. Saad and M. H. Schultz. GMRES: A generalized minimal residual algorithm for solving non-symmetric linear systems. *SIAM Journal on Scientific and Statistical Computing*, 7(3):856–869, 1986.
- M. S. Alnæs. *UFL: a Finite Element Form Language*, chapter 17. Springer, 2012.
- X. Zhang and C. W. Shu. Maximum-principle-satisfying and positivity-preserving high-order schemes for conservation laws: survey and new developments. *Proceedings of the Royal Society A: Mathematical, Physical and Engineering Sciences*, 467(2134):2752–2776, 2011.